

Bayesian Constrained Energy Minimization for Hyperspectral Target Detection

Jing Zhang, Rui Zhao, and Zhenwei Shi^{*} *Member, IEEE*, Ning Zhang, Xinzong Zhu

Abstract—For better performance of hyperspectral target detectors, the prior target spectrum is expected to be accurate and consistent with the target spectrum in the hyperspectral image to be detected. The existing hyperspectral target detection algorithms usually assume that the prior target spectrum is highly reliable. However, the label obtained is not always precise in practice and pixels of the same object may have quite different spectra. Since it is hard to acquire a highly reliable prior target spectrum in some application scenarios, we propose a Bayesian Constrained Energy Minimization method (B-CEM) for hyperspectral target detection. Instead of the point estimation of the target spectrum, we infer the posterior distribution of the true target spectrum based on the prior target spectrum. Specifically, considering the characteristics of hyperspectral image and target detection task, we adopt the Dirichlet distribution to approximate the true target spectrum. Experimental results on three datasets demonstrate the effectiveness of the proposed B-CEM when the known target spectrum is noisy or inconsistent with the true target spectrum. The necessity to approximate the true target spectrum is also proved. Generally, distributional estimate achieves better performance than using the known target spectrum directly.

Index Terms—Bayesian, distributional estimate, hyperspectral target detection.

I. INTRODUCTION

HYPERSPECTRAL remote sensing image contains abundant spectral and spatial information and has been widely used both in the military and civilian fields, such as national defense [1], [2], security [3], mineralogy [4], and agriculture [5]. Hyperspectral target detection, which is a significant task in HSI processing, is gradually attracting increasing attention. It can be applied to detect important military targets [6], [7], such as oil tanks, aircraft, ships, and airports. Besides, it can also be used to detect newborn leaves [8], iron oxide [9], gas [10], and post-disaster rescue [11]. In recent years, hyperspectral target detection algorithms have been studied extensively and deeply.

Existing hyperspectral target detection methods are primarily based on spectral information and simple correlation

The work was supported by the National Key R&D Program of China under the Grant 2019YFC1510905, the National Natural Science Foundation of China under the Grant 61671037, the Beijing Natural Science Foundation under the Grant 4192034 and Shanghai Association for Science and Technology under the Grant SAST2020077. (*Corresponding author:* Zhenwei Shi (*e-mail:* shizhenwei@buaa.edu.cn))

Jing Zhang, Rui Zhao and Zhenwei Shi are with Image Processing Center, School of Astronautics, Beihang University, Beijing 100191, China, and with Beijing Key Laboratory of Digital Media, Beihang University, Beijing 100191, China, and also with State Key Laboratory of Virtual Reality Technology and Systems, School of Astronautics, Beihang University, Beijing 100191, China.

Ning Zhang and Xinzong Zhu are with Shanghai Aerospace Electronic Technology Institute, Shanghai 201109, China.

information of adjacent pixels to complete detection tasks. The most direct idea is to measure the distance between the spectrum of the tested pixel and the prior spectrum of the target and then to detect the target. The spectral angle mapper (SAM) [12] measures the spectral angle between the spectrum of the test pixel and the prior spectral features of the target as the distance. The spectral information divergence (SID) [13] algorithm leverages the relative entropy to interpret spectral information and compares the similarity between the two spectra by measuring the probabilistic discrepancy between them.

Since the above hyperspectral target detection algorithms only require prior knowledge of the target spectral features, their performance usually depends on the quality of the prior target features [14]. Some methods use prior knowledge of the spectral signature of both target and background. Matched filter (MF) [15], adaptive matched filter (AMF) [16], [17] and adaptive coherence/cosine estimator (ACE) [15], [18], [19] are detection algorithms based on binary hypothesis test. AMF and ACE are based on the target and background spectrum following the assumption of different Gaussian distribution probability models, and the detector is derived from the generalized-likelihood ratio test (GLRT) [20]. In [21], a new SNR-based signal detection theory is developed and LRT/GLRT-derived detectors can be interpreted as SNR/GSNR-derived detectors where no probability distributions are assumed. Moreover, the adaptive cosine estimator (ACE) can be also shown to be a special case of an SA-detector based on the new SA-based signal detection theory in conjunction with data whitening.

Another classical hyperspectral target detection algorithm is based on the subspace model. The orthogonal subspace projection (OSP) [22], [23] first projects the spectrum of the test pixel to the orthogonal subspace of the background's spectrum to suppress the interference of the background's spectrum. Then it finds a vector with the maximum of the residual target signature SNR. However, the performance of the orthogonal subspace projection (OSP) is sensitive to the prior target knowledge, and the prior target knowledge is significantly affected by the target background. To address this issue, Chang et al. [24] develop three approaches to extend OSP in improving its performance, namely data spherizing, BKG-annihilated OSP (BA-OSP) based on LRaSMD, and a combination of data spherizing and LRaSMD. Besides, hyperspectral target detection algorithms based on sparse representation [25], [26] establish an overcomplete spectral dictionary containing target and background spectral features, and assume that the spectrum of each pixel can be represented as a sparse linear combination of the spectrum contained in the

spectral dictionary. Then target detection is transformed into an \mathcal{L}_0 norm minimization problem. In order to achieve the separation of the target and the background, the Constrained Energy Minimization (CEM) [22], [27] utilizes a finite impulse response (FIR) filter that minimizes the total spectral output energy with constrain of outputting a constant filter's response to the target spectral feature. Based on these methods, some latest methods are presented, such as the Robust CEM [28], the Hierarchical CEM (H-CEM) [29], the Ensemble-Based Cascaded CEM (E-CEM) [30], the automatic target detection and classification algorithm (ATDCA) [31], Matched Shrunken Subspace Detectors (MSSD) [32], etc.

The prior knowledge of the spectral features of target and background is difficult to obtain in practical applications. It is even more difficult to obtain complete statistical features of the background spectrum. Therefore, spatial correlation and simple texture information are added in [33], [34] to improve the detection performance. TVHTD algorithm [35] utilizes the total variation to take advantage of the spatial information of the hyperspectral image. Besides, several band selection algorithms have been proposed for target detection. Xu et al. [36] propose a particle swarm optimization (PSO)-based band selection (BS) approach. Chang et al. [37] reinterpret the CEM-CBS as linearly constrained minimum variance-based CBS (LCMV-CBS).

In recent years, the idea of machine learning has been introduced into hyperspectral target detection. For example, the Ensemble-Based Cascaded CEM (E-CEM) [30] introduces the idea of ensemble learning, which to some extent alleviates the overfitting problem of nonlinear or layered detectors based on partial spectral data, and gets detectors with relatively stable performance. Random forest-based metric learning detector [38] is also proposed. Moreover, several cascaded detection algorithms, such as the Hierarchical CEM (H-CEM) [29] and the Robust Iteratively Reweighted Unstructured Detector (RACE) [14], have been proposed. There are also some other efforts contributing to improving HTD techniques, such as structurally incoherent background and target dictionaries (SIBTD) [39] and kernel-based SAM [40]. In addition, deep convolutional neural network is also adopted to process target detection tasks [41].

Existing hyperspectral target detection algorithms usually assume that the spectral features of the target are highly reliable. However, this assumption is not always valid. On one hand, the known target spectrum is always obtained by averaging all spectra of all pixels of the target object according to the label of the hyperspectral image for a similar scene, which further assumes that the label of the data set is highly reliable. Since a large number of ground investigations and abundant prior knowledge about the scene captured is a must to accurately label the hyperspectral image [42], the label obtained by visual interpretation is not always precise in practice. Spontaneous mixing of data distribution may also lead to sample crossover between different classes. On the other hand, the quality of the spectral data can not always be guaranteed because it is vulnerable to uncompensated errors in the sensor, surface contaminants, material diversity, light shadows, weather, and other environmental factors. In this case

of imperfection, the spectral properties of the pixels in the hyperspectral image are usually quite complex, meaning that pixels of the same object may have quite different spectra. For example, to detect the aircraft, the spectrum of the target aircraft at airport A was captured yesterday morning and stored in the spectrum library as the known target spectrum. Our task is to detect the same type of aircraft at airport B this afternoon, where the true target spectrum is considered to be the spectrum of the aircraft captured at airport B this afternoon. The true target spectrum is inconsistent with the known target spectrum.

Therefore, the common and inevitable problems in the target detection task for the hyperspectral image are as follows: 1) There is noise in the known spectrum of the target; 2) The target spectrum of the given hyperspectral image is not consistent with the known target spectrum. Since the quality of the prior target spectrum is significant for the hyperspectral target detectors [14], the above problems can seriously degrade the detection performance.

In this work, we introduce the true spectrum of targets as an intermediate variable for the purpose to enhance the robustness of the method for the possible noise in the known target spectrum or the spectral inconsistency between the true target spectrum and the given target spectrum. There are primarily two methods for estimating variables, namely point estimation and distribution estimation. Point estimation is to obtain a specific value of the true target spectrum by leveraging the known target spectrum, while distribution estimation is to infer the distribution that the true target spectrum may follow according to the known target spectrum and its confidence. Compared with point estimation, distribution estimation is not only based on the known target spectrum, but also takes into account the distribution that the target spectrum may follow. Since only one possible spectrum of the target is available, instead of the point estimation, we aim to infer the posterior distribution of the true target spectrum to effectively handle its uncertainty. Then a Bayesian Constrained Energy Minimization method (B-CEM) is developed for hyperspectral target detection. Specifically, we adopt the Dirichlet distribution to estimate the true target spectrum. Two major reasons contribute to this proposal: 1) Hyperspectral images are generally considered to follow a mixture of Gaussian distributions. 2) Given that the background of the hyperspectral image \mathbf{X} is unknown, no one knows how many Gaussian distributions produced the data, and hence the number of clustering cannot be determined. The experimental results prove the effectiveness of our proposed approach against competitive methods.

The contributions of our work are as follows:

- 1) We note that the exact target spectrum is not always available, which means the known target spectrum is noisy or inconsistent with the true target spectrum. Hence, we introduce Bayesian to hyperspectral target detection and formalize the problem in a probabilistic way.
- 2) We introduce the true target spectrum as an intermediate variable, and develop a hierarchical probability model. We adopt distributional estimation for the true target spectrum to overcome the uncertainty caused by the difficulties to label the hyperspectral image accurately and the unstable quality of the spectral data.

The rest of this paper is organized as follows. In section II, we give a process of probabilistic inference in detail and introduce our proposed target detection method (B-CEM) for hyperspectral image. Details about data sets and some experimental results are reported in section III. The conclusions are given in Section IV.

II. METHODOLOGY

We divide hyperspectral target detection into two steps: 1) estimation of the true target spectrum, and 2) target detection. In the first stage, we aim at acquiring the approximate posterior distribution over the true target spectrum so as to acquire better detection performance. Specifically, we consider the known target spectrum as the mean of the Gaussian distribution, the variance of which depends on the confidence of the known target spectrum. Once the Gaussian distribution is obtained, we treat it as the base distribution of the Dirichlet distribution and adopt the Dirichlet distribution to approximate the posterior distribution over the true target spectrum. In the second stage, we adopt a regularized CEM detector to detect targets with the true target spectrum sampled from the Dirichlet distribution acquired in the first stage and infer the posterior detection score over an unknown background.

In this section, we review the classical CEM detector and the regularized CEM detector [43] briefly in subsection A. Then we detail the proposed methods, B-CEM. The true target spectrum is introduced as an intermediate variable and the detection score is factorized then in subsection B. Therefore, the key is turned to acquire the true distribution for the true target spectrum. Since the true distribution for the true spectrum is hard to solve directly, we take an amortized variational inference approach to approximate the posterior. Specifically, we propose to formulate the distribution as a Dirichlet one and present two major reasons that contribute to this proposal in subsection C. Unfortunately, the expression of the closed-form of the Dirichlet distribution cannot be derived. The process to obtain a specific Dirichlet distribution hence is introduced in detail in subsection D.

A. CEM Detector

For HSI data set $\mathbf{X} = [\mathbf{x}_1, \dots, \mathbf{x}_N] \in \mathbb{R}^{C \times N}$, $\mathbf{x}_i \in \mathbb{R}^{C \times 1}$ is the spectrum of pixel i , C is the number of the bands, N is the total number of pixels. Except for the hyperspectral image, the target spectrum $\mathbf{t} \in \mathbb{R}^{C \times 1}$ is also available.

CEM can be considered as a standard linear filter. The filter's response to the target spectral feature is the inner product of the spectrum vector \mathbf{x} and detector's coefficient ω :

$$\mathbf{y} = \mathbf{w}^T \mathbf{X} \quad (1)$$

In order to separate the target from the background, CEM aims to find a projection vector that keeps the output of the target large and suppresses the output of the background.

The optimal coefficients of a CEM detector can be obtained by minimizing the average “energy” of output, which can be obtained by averaging the square of the output values, under

the constrain that the filter's response to the target spectral feature is a constant:

$$\begin{aligned} \min_{\mathbf{w}} E[\mathbf{y}^2] &= \mathbf{w}^T \mathbf{R} \mathbf{w} \\ \text{s. t. } \mathbf{w}^T \mathbf{t} &= 1 \end{aligned} \quad (2)$$

where $\mathbf{R} = E[\mathbf{XX}^T] = \frac{1}{N} \mathbf{XX}^T \in \mathbb{R}^{C \times C}$ is the maximum likelihood estimation of correlation matrix for the HSI data set X . The closed solution of the above optimization problem can be given as follow:

$$\mathbf{w}^* = \frac{\mathbf{R}^{-1} \mathbf{t}}{\mathbf{t}^T \mathbf{R}^{-1} \mathbf{t}} \quad (3)$$

Due to the performance of CEM in the target detection task of hyperspectral images, many methods have been devoted to improving the performance of the detector based on CEM in recent years. A classic improvement is the regularized CEM detector.

Adding a positive diagonal matrix with small values $\lambda \mathbf{I}$ to the matrix \mathbf{R} : $\mathbf{R} + \lambda \mathbf{I}$, where $\lambda > 0$, can help enhance the numerical stability of matrix inverse operation \mathbf{R}^{-1} . Then the closed solution of the CEM detector can be modified as:

$$\mathbf{w}(\lambda)^* = \frac{(\mathbf{R} + \lambda \mathbf{I})^{-1} \mathbf{t}}{\mathbf{t}^T (\mathbf{R} + \lambda \mathbf{I})^{-1} \mathbf{t}} \quad (4)$$

Once we obtain the optimal coefficients of the CEM detector $\mathbf{w}(\lambda)^*$, Equation 1 can be adopted to complete the detection on each pixel of X .

B. Detection Score Expression

We use Bayesian in hyperspectral target detection and transform regularized CEM detector into a filter. Given a hyperspectral image \mathbf{X} to be detected and the known target spectrum \mathbf{t}_{obs} , we compute the following detection score:

$$f(\mathbf{x}_i | \mathbf{t}_{obs}, \lambda) = (\mathbf{w}(\lambda)^*)^T \mathbf{x}_i \quad (5)$$

where x_i is one of the pixels in the hyperspectral image X , \mathbf{t}_{obs} is the known spectrum of the target of interest, $\lambda > 0$ is the regularization coefficient and $(\mathbf{w}(\lambda)^*)^T$ is the optimal coefficients of the regularized CEM detector obtained by Equation 4.

However, the common and inevitable problems in the target detection task for the hyperspectral image are as follows: 1) There is noise in the known spectrum of the target; 2) The target spectrum \mathbf{t}_{true} of the given hyperspectral image \mathbf{X} is not consistent with the known target spectrum \mathbf{t}_{obs} .

Therefore, we introduce the true target spectrum \mathbf{t}_{true} as an intermediate variable to enhance the robustness of the method for 1) the possible noise in \mathbf{t}_{obs} or 2) the spectral inconsistency between \mathbf{t}_{obs} and \mathbf{t}_{true} . We draw on the detection processes that humans perform in hyperspectral target detection tasks. When we are to detect the target in the hyperspectral image \mathbf{X} and given the known target spectrum \mathbf{t}_{obs} , the first step is to get the true target spectrum \mathbf{t}_{true} , which is consistent with the target spectrum of the hyperspectral image \mathbf{X} .

Since the true target spectrum \mathbf{t}_{true} is hard to obtain directly, our method models the posterior distribution for \mathbf{t}_{true}

based on the known target spectrum \mathbf{t}_{obs} , which is represented as $p(\mathbf{t}_{true} | \mathbf{t}_{obs})$. Given that only one possible spectrum of the target is available, distributional estimates rather than point estimates are used. By introducing the true target spectrum \mathbf{t}_{true} , the detection score can be obtained by:

$$\begin{aligned}\tilde{f}(\mathbf{x}_i | \mathbf{t}_{true}, \lambda) \\ = \int f(\mathbf{x}_i | \mathbf{t}_{true}, \lambda) \cdot p(\mathbf{t}_{true} | \mathbf{t}_{obs}) d\mathbf{t}_{true}\end{aligned}\quad (6)$$

C. Approximation of the Posterior Distribution

Since the known target spectrum \mathbf{t}_{obs} is not always clean and may not be exactly the same as the spectrum of targets in the hyperspectral image \mathbf{X} , we introduce the true target spectrum \mathbf{t}_{true} as an intermediate variable and develop a bayesian constrained energy minimization method (B-CEM). Unfortunately, the true distribution for the true spectrum $p(\mathbf{t}_{true} | \mathbf{t}_{obs})$ is hard to solve directly, our approach takes an amortized variational inference approach to approximate the posterior. Specifically, the Dirichlet distribution is finally adopted for the approximate posterior distribution over the true target spectrum $q(\mathbf{t} | \mathbf{t}_{obs}, \alpha)$ in this work, where α is the parameter of the Dirichlet distribution $G \sim \mathcal{DP}(\alpha, G_0)$. Two major reasons contribute to this proposal: 1) Hyperspectral images are generally considered to follow a mixture of Gaussian distributions. 2) Given that the background of the hyperspectral image \mathbf{X} is unknown, no one knows how many Gaussian distributions produced the data, and hence the number of clustering cannot be determined. For the base distribution G_0 of the Dirichlet distribution $G \sim \mathcal{DP}(\alpha, G_0)$, we consider the known target spectrum \mathbf{t}_{obs} as the mean of the Gaussian distribution G_0 , the variance var of which depends on the confidence of \mathbf{t}_{obs} . The higher the confidence, the smaller the variance var . Based on the Gaussian distribution $G_0 \sim \mathcal{N}(\mathbf{t}_{obs}, var)$, we assume that the approximate true target spectrum \mathbf{t} follows the obtained Dirichlet distribution $G \sim \mathcal{DP}(\alpha, G_0)$.

As mentioned above, we represent the approximate posterior distribution over the true target spectrum $G \sim \mathcal{DP}(\alpha, G_0)$, where $G_0 \sim \mathcal{N}(\mathbf{t}_{obs}, var)$ as $q(\mathbf{t} | \mathbf{t}_{obs}, \alpha)$. The detection score of each pixel \mathbf{x}_i in the hyperspectral image \mathbf{X} hence can be approximated by the approximate true target spectrum \mathbf{t} as follow:

$$\begin{aligned}\tilde{f}(\mathbf{x}_i | \mathbf{t}_{true}, \lambda) \\ \approx \int f(\mathbf{x}_i | \mathbf{t}, \lambda) \cdot q(\mathbf{t} | \mathbf{t}_{obs}, \alpha) d\mathbf{t}\end{aligned}\quad (7)$$

D. Approximation of the True Target Spectrum

The approximate true target spectrum \mathbf{t} follows the obtained Dirichlet distribution $G \sim \mathcal{DP}(\alpha, G_0)$, which is a distribution over probability distributions and is determined by two parameters α, G_0 . α is a positive concentration or scaling parameter, the smaller the value is, the more concentrated the distribution is. $G_0 \sim \mathcal{N}(\mathbf{t}, var)$ is the base Gaussian distribution. Therefore, the Dirichlet Process \mathcal{DP} can be considered as a black box, where the input distribution is G_0 , the output distribution is G , and α controls what the output

looks like. G is a random probability measure that has the same support as G_0 . If $G \sim \mathcal{DP}(\alpha, G_0)$, for any finite set of partitions $\mathbf{X}_1 \cup \mathbf{X}_2 \cup \dots \cup \mathbf{X}_k$ of \mathbf{X} , we have

$$G(\mathbf{X}_1), \dots, G(\mathbf{X}_k) \sim Dirichlet(\alpha G_0(\mathbf{X}_1), \dots, \alpha G_0(\mathbf{X}_k)) \quad (8)$$

where $G(\mathbf{X}_i)$ is the sum of the probabilities of this discrete distribution of G within partition \mathbf{X}_i , $G_0(\mathbf{X}_i)$ is the sum of the probability of base distribution G_0 within partition \mathbf{X}_i .

Unfortunately, the closed-form solution of the Dirichlet distribution G cannot be derived. Therefore, the process to sample G , which is graphically known as stick-breaking, is detailed following. Firstly, we sample $\theta_1 \sim G_0$ and $\beta_1 \sim Beta(1, \alpha)$, then $\pi_1 = \beta_1$. Then we sample the first sample and set the weight of this sample to β_1 . Similarly, we sample $\theta_2 \sim G_0$ and $\beta_2 \sim Beta(1, \alpha)$, then $\pi_2 = (1 - \pi_1) \times \beta_2$. We sample the second sample and set the weight of this sample to β_2 . This stick should have $1 - \pi_1 - \pi_2$ left then and we continue to take β_3 from it. Then $\pi_3 = (1 - \pi_1 - \pi_2) \times \beta_3$. In this way, G is obtained. θ_i is the position and π_i is the weight. Since the whole process is like breaking the stick, the sampling process to get the Dirichlet distribution G is called stick breaking.

We formulate the approximate posterior distribution over the true target spectrum $q(\mathbf{t} | \mathbf{t}_{obs}, \alpha)$ as the Dirichlet distribution $G \sim \mathcal{DP}(\alpha, G_0)$. Once a specific G obtained by stick breaking is acquired, we will sample 10 spectral signatures as the set of true target spectra $\mathbf{T} = \{\mathbf{t}_1, \mathbf{t}_2, \dots, \mathbf{t}_{10}\}$ from it.

Given each approximate true target spectrum $\mathbf{t}_i \in \mathbf{T}$ and the hyperspectral image $\mathbf{X} = [\mathbf{x}_1, \dots, \mathbf{x}_N] \in \mathbb{R}^{C \times N}$, we adopt a regularized CEM detector to detect targets from an unknown background and get the target detection score:

$$f(\mathbf{x}_i | \mathbf{t}_i, \lambda) = (\mathbf{w}(\lambda)^*)^T \mathbf{x}_i \quad (9)$$

where

$$\mathbf{w}(\lambda)^* = \frac{(\mathbf{R} + \lambda \mathbf{I})^{-1} \mathbf{t}_i}{\mathbf{t}_i^T (\mathbf{R} + \lambda \mathbf{I})^{-1} \mathbf{t}_i} \quad (10)$$

Therefore, the final target detection score can be derived:

$$\tilde{f}(\mathbf{x}_i | \mathbf{t}_{true}, \lambda) \approx \frac{1}{10} \sum_{i=1}^{10} f(\mathbf{x}_i | \mathbf{t}_i, \lambda), i = 1, 2, \dots, 10 \quad (11)$$

where $\mathbf{t}_i \in \mathbf{T}$.

III. EXPERIMENT

We compare the proposed B-CEM with six other algorithms on hyperspectral target detection tasks and prove the effectiveness of our method. Since the label obtained is not always precise in practice and pixels of the same object may have a quite different spectrum, there is always noise in the known target spectrum or a gap between the known target spectrum and the true target spectrum in the real application scenario. The known target spectra of the experimental data sets are considered as the true target spectra because they are obtained by averaging the target spectra in the test scene. However, this is impossible in practice and we cannot acquire such a true target spectrum in the real application scenario because a gap often exists between the known target spectrum and the true target spectrum. Therefore, to evaluate whether our method can address this issue which always occurs in practice, we

have to simulate the gap between the known target spectrum and the true target spectrum. In this paper, we use a simple way to simulate the gap, namely adding noise. We consider the target spectra, which are obtained by averaging the target spectra in the test scene, as the true target spectra t_{true} . Then we add noise to the true target spectra as the known target spectra t_{obs} , which can be obtained in real-world applications. Specifically, we add Gaussian white noise with a Signal-to-Noise Ratio (SNR) of $10dB - 50dB$ to the target spectrum. The higher the SNR, the less the noise is contained in the known target spectrum. SNR refers to the ratio of signal energy and quantization noise energy. The calculation formula of SNR is as follows:

$$\text{SNR(dB)} = 10 \log_{10} \left(\frac{P_{\text{signal}}}{P_{\text{noise}}} \right) = 20 \log_{10} \left(\frac{A_{\text{signal}}}{A_{\text{noise}}} \right) \quad (12)$$

where P_{signal} is the power of signal, P_{noise} is the power of noise, A_{signal} is the amplitude of signal, and A_{noise} is the amplitude of noise. We can draw a conclusion from the formula of SNR that the lower SNR is, the greater the noise is.

We evaluate the detection performance of six other detectors and our B-CEM under different SNR. All the experiments are conducted using python on a workstation with an Intel(R) Core(TM) i7-10700K processor (3.80 GHz), 64 GB of memory, and Nvidia GeForce RTX 2080 Ti.

A. Datasets

We conduct experiments on one synthetic hyperspectral image generated from the United States Geological Survey (USGS) digital spectral library [44], and two real hyperspectral images, AVIRIS San Diego Data, and AVIRIS Cuprite Data.

The synthetic hyperspectral image consists of 15 kinds of endmember spectrum. Similarly to Chang et al. [45], we divide the synthetic map with size of $s^2 \times s^2$, $s = 8$ into $s \times s$ regions. Then we initialize each region with the same type of ground cover randomly selected from the aforementioned 15 kinds of spectra. By replacing the spectrum of background pixels, we implant the target into the corresponding pixels. In order to ensure that there is no pure pixel in this hyperspectral image synthesized, the synthetic data is mixed through a $(s+1) \times (s+1)$ spatial low-pass filter. The other detailed information is shown in Table I. The first band of the synthetic hyperspectral image and the ground truth location of the target are shown in Figure 1.

The AVIRIS San Diego data set, which is collected by AVIRIS at San Diego, America, contains a part of an airport. The target of interest in this image is the three airplanes. The spectrum of the target is obtained by averaging all spectra of pixels in the target regions. The other detailed information is shown in Table I. The first band of the hyperspectral image and the ground truth location of the target are shown in Figure 2.

The AVIRIS Cuprite Data, which is collected by AVIRIS in the Cuprite mining district of Nevada, contains about 14 kinds of mineral in this image. A subset of this image with 250×191 pixels are used to evaluate our method and are marked by

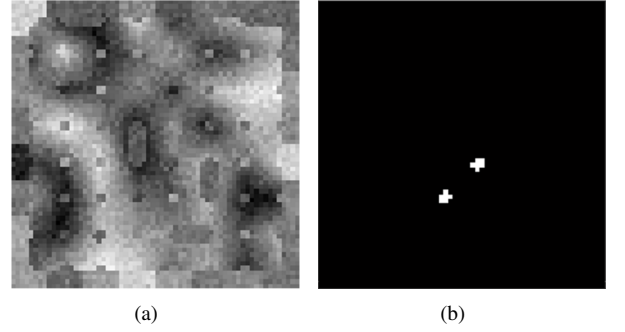


Fig. 1: The synthetic hyperspectral image. (a) The first band of the synthetic hyperspectral image. (b) The ground truth.

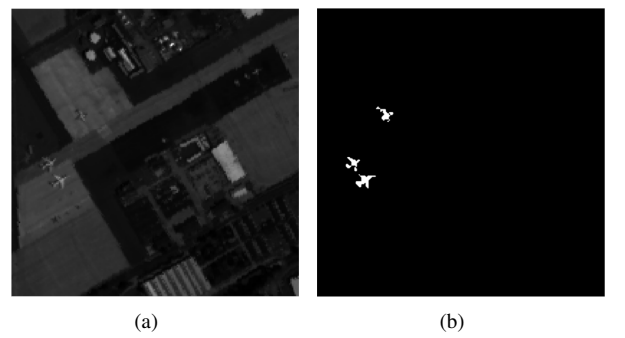


Fig. 2: The AVIRIS San Diego hyperspectral image. (a) The first band of the synthetic hyperspectral image. (b) The ground truth.

the red box in Figure 3 (a), which is the minerals map [46] produced by the Tricorder 3.3 software. The other detailed information is shown in Table I, where the number of bands used is 188 after removing the low SNR and water absorption bands. Since the target of interest in this hyperspectral image, the buddingtonite, has two kinds of spectrum in the USGS Digital Spectral Library [44], we make the target spectrum be the average of them. The first band of the hyperspectral image and the ground truth location of the target are shown in Figure 3.

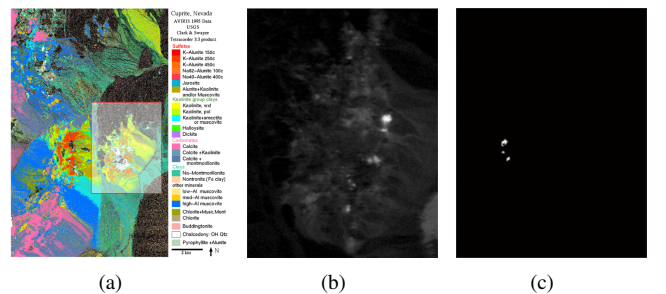


Fig. 3: The AVIRIS Cuprite hyperspectral image. (a) The AVIRIS Cuprite hyperspectral image and its subset used. (b) The first band of the synthetic hyperspectral image. (c) The ground truth.

TABLE I: Detailed information of data sets used. Syn is the synthetic hyperspectral image, San is the AVIRIS San Diego Data, and Cup is the AVIRIS Cuprite Data.

| Dataset | No. of band used | Wavelength | No. of target pixels | Target | Size |
|---------|------------------|--------------|----------------------|---------------------------------------|-----------|
| Syn | 224 | 400 – 2500nm | 12 | The Labradorite HS17.3B | 64 × 64 |
| San | 189 | 380 – 2510nm | 134 | The average within the target regions | 200 × 200 |
| Cup | 188 | 400 – 2500nm | 39 | The buddingtonite | 250 × 191 |

B. Detection performance

We compare the detection performance of B-CEM with the Constrained Energy Minimization (CEM) [27], the adaptive coherence/cosine estimator (ACE) [18], the Matched filter (MF) [15], the spectral information divergence (SID) [13], the spectral angle mapper (SAM) [12] and the Ensemble-Based Cascaded CEM E-CEM [30], including classical detection algorithms and the SOTA method. As mentioned earlier, Gaussian white noise with different SNR is added to the true target spectrum t_{true} to simulate the situation where t_{obs} is noisy or not exactly the same as t_{true} .

In order to more intuitively reflect the magnitude of added noise with SNR range from 10dB to 50dB, we visualized the target spectrum t_{true} of the AVIRIS San Diego data set and the target spectrum t_{obs} with noise of 10dB, 30dB and 50dB, which is shown in Figure 4. It can be observed that when SNR is greater than 30dB, the target spectrum with noise added is relatively close to the known target spectrum. Therefore, we only present detection results and ROC curves on the three data sets when SNR ranges in 10dB – 30dB.

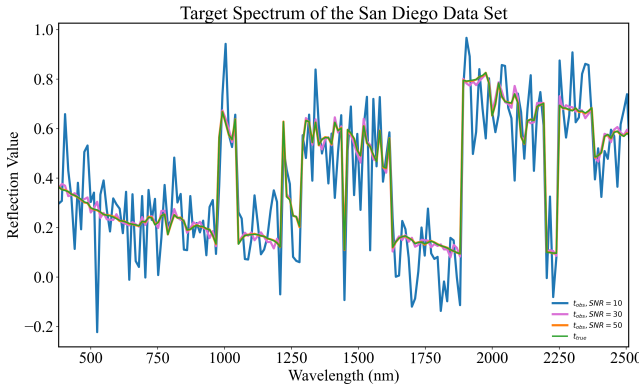


Fig. 4: The true target spectrum t_{true} and the target spectrum t_{obs} with noise of 10dB, 30dB and 50dB. When SNR is greater than 30, the target spectrum with noise added is relatively close to the original target spectrum.

1) *Detection performance on the AVIRIS San Diego data set:* The corresponding numerical AUC with the noisy known target spectrum when the SNR (Signal-to-Noise Ratio) ranges from 10dB – 50dB for six other detectors and our B-CEM are reported in Table II in detail. Figure 5 and Figure 6 show the detection results and ROC Curve with the noisy known target spectrum when the SNR ranges from 10dB – 30dB.

The numerical AUC with SNR ranging from 10dB – 50dB, which is presented in Table II, demonstrates that B-CEM gets a significant performance boost compared with other detectors.

TABLE II: AUC of the different methods on the San Diego Data Set. The known spectrum of the target t_{obs} contains Gaussian white noise of SNR ranges in 10dB – 50dB. Best results are highlighted in bold.

| | SNR = 10 | SNR = 20 | SNR = 30 | SNR = 40 | SNR = 50 |
|--------------|--------------|--------------|--------------|--------------|--------------|
| CEM [27] | 49.89 | 46.97 | 45.64 | 61.45 | 76.79 |
| ACE [18] | 44.38 | 45.19 | 48.16 | 40.86 | 59.22 |
| MF [15] | 47.79 | 45.55 | 45.04 | 63.44 | 76.23 |
| SID [13] | 83.04 | 82.70 | 81.82 | 81.36 | 81.12 |
| SAM [12] | 85.57 | 81.23 | 81.06 | 80.89 | 80.47 |
| E-CEM [30] | 59.76 | 61.69 | 58.21 | 52.77 | 64.28 |
| B-CEM | 96.34 | 98.69 | 98.42 | 98.42 | 98.42 |

In B-CEM, we assume that the known target spectrum t_{obs} is often noisy or not exactly the same as the true target spectrum. Based on the assumption above, we introduce t as an intermediate variable to estimate the true target spectrum and infer its approximate posterior distribution. Since the target spectrum with high SNR is close to the known target spectrum, our hypothesis that the known target spectrum is not consistent with the true spectrum is not valid. Therefore, the detection performance of B-CEM drops slightly when SNR is 30dB or higher. While a quite low SNR (for example, 10dB) maybe means that the obtained approximate posterior distribution over the true target spectrum contains noise, which probably leads to the degradation of detection performance. However, the detection performance of B-CEM is significantly superior to that of other detectors despite the variation of SNR. Besides, the performance gap of B-CEM with different SNRs is small.

A similar conclusion can be drawn from the visualization of the detection results. At high noise levels (SNR is 10dB), two aircraft can be detected by B-CEM. When the noise is not as much (SNR is 20dB and 30dB), B-CEM can detect all three aircraft. B-CEM has a better detection ability compared with other methods. It is worth noting that CEM [27], the basis of our B-CEM, acquires a relatively poor performance, which demonstrates the advantage of the distribution estimation and the effectiveness of the proposed method.

Receiver Operating Characteristic (ROC) Curve is shown in Figure 6 and proves the effectiveness of the proposed B-CEM detector. The performance of B-CEM when SNR is 20dB and 30dB is superior to that when SNR is 10dB. Regardless of the SNR of noise contained in the known target spectrum t_{obs} , B-CEM acquires obviously better performance compared to other detectors. However, 2D ROC curve can not evaluate the target detectability and also not background suppressibility (BS) [47]. For this reason, we further evaluate the detection

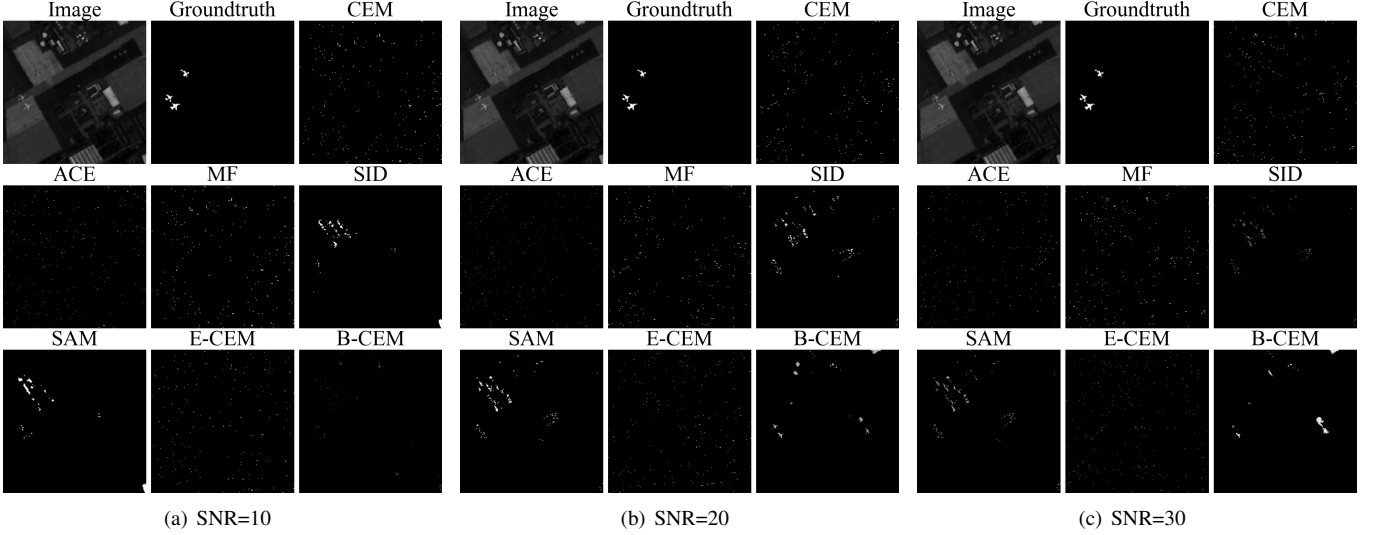


Fig. 5: The detection results of detectors on the AVIRIS San Diego data set with the noisy known target spectrum. SNR (Signal-to-Noise Ratio) ranges from $10dB - 30dB$.

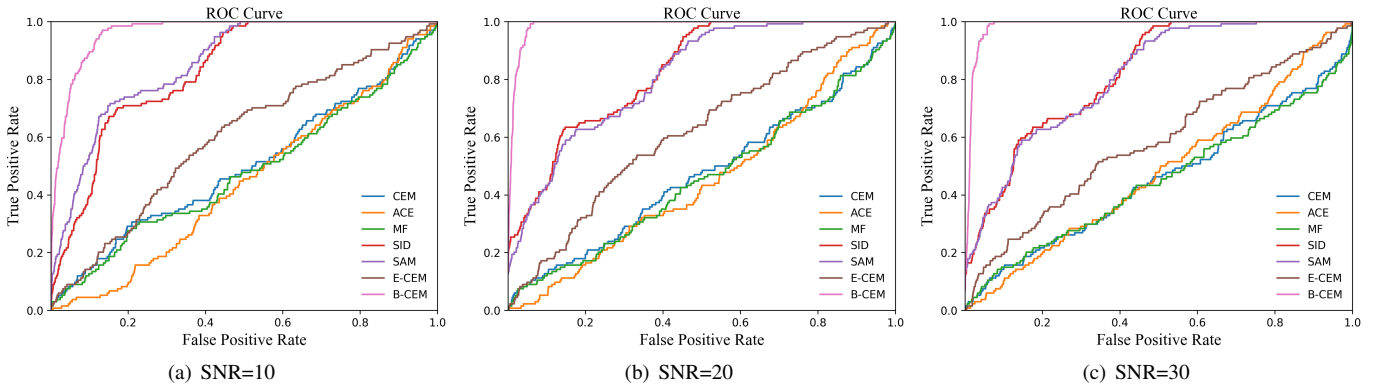


Fig. 6: The ROC Curves of detectors on the AVIRIS San Diego data set with the noisy known target spectrum. SNR (Signal-to-Noise Ratio) ranges from $10dB - 30dB$.

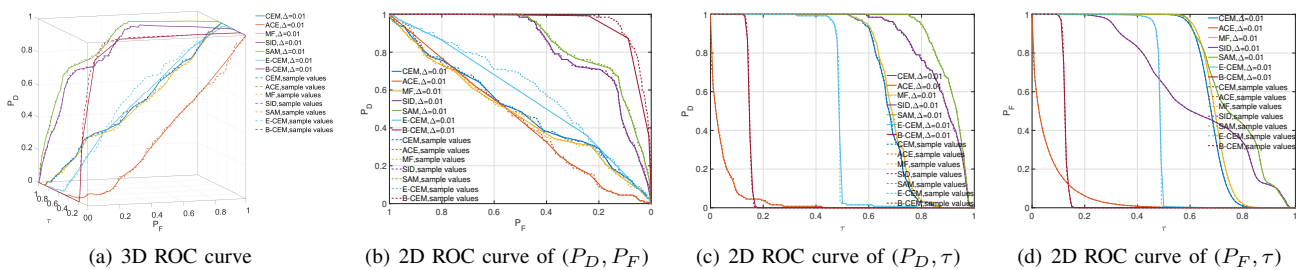


Fig. 7: 3D ROC curves along with its generated three 2D ROC curves using Equation 13 by data sample values and uniform step size, $\Delta = 0.01$, on the San Diego data Set with the noisy known target spectrum when $SNR = 10$

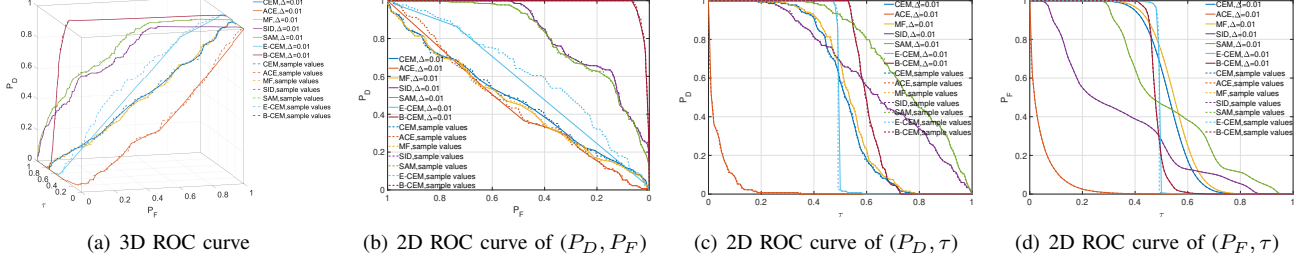


Fig. 8: 3D ROC curves along with its generated three 2D ROC curves using Equation 13 by data sample values and uniform step size, $\Delta = 0.01$, on the San Diego data Set with the noisy known target spectrum when SNR = 20

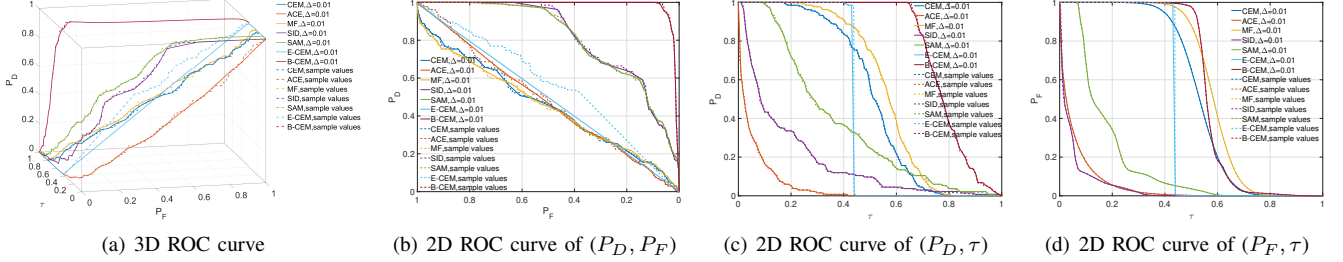


Fig. 9: 3D ROC curves along with its generated three 2D ROC curves using Equation 13 by data sample values and uniform step size, $\Delta = 0.01$, on the San Diego data Set with the noisy known target spectrum when SNR = 30

performance of our method by the 3D ROC curves proposed in [47]. We adopt the detector as follow:

$$\delta_{\tau}^{\text{NP}}(\mathbf{t}_{\text{obs}}) = \begin{cases} 1; & \text{if } \delta_{\text{normalized}}^{\text{NP}}(\mathbf{t}_{\text{obs}}) > \tau \\ 0; & \text{if } \delta_{\text{normalized}}^{\text{NP}}(\mathbf{t}_{\text{obs}}) \leq \tau \end{cases} \quad (13)$$

where

$$\delta_{\text{normalized}}^{\text{NP}}(\mathbf{t}_{\text{obs}}) = \frac{\delta_{\tau}^{\text{NP}}(\mathbf{t}_{\text{obs}}) - \min_{\mathbf{t}_{\text{obs}}} \delta_{\tau}^{\text{NP}}(\mathbf{t}_{\text{obs}})}{\max_{\mathbf{t}_{\text{obs}}} \delta_{\tau}^{\text{NP}}(\mathbf{t}_{\text{obs}}) - \min_{\mathbf{t}_{\text{obs}}} \delta_{\tau}^{\text{NP}}(\mathbf{t}_{\text{obs}})} \quad (14)$$

Figure 7-9(a) present the 3D ROC Curves when SNR ranges in $10dB - 30dB$, which is generated as a function of (P_D, P_F, τ) with three independent variable. τ is the threshold parameter, P_D is detection probability and P_F is false alarm probability. Figure 7-9(b) shows the 2D ROC curves of (P_D, P_F) derived from 3D ROC curve. Their corresponding AUC values can be further used to evaluate the effectiveness of detectors with SNR ranging in $10dB - 30dB$. Figure 7-9(c) shows the 2D ROC curves of (P_D, τ) derived from 3D ROC curve. Their corresponding AUC values can be further used to evaluate detection probability of detectors. Higher values of $AUC_{(D,F)}$ and $AUC_{(D,\tau)}$ indicate higher detection performance. Figure 7-9(d) shows the 2D ROC curves of (P_F, τ) derived from 3D ROC curve. Their corresponding AUC values can be further used to evaluate background suppression of detectors. A lower value of $AUC_{(F,\tau)}$ indicates a better BKG suppression and thus a better detection performance.

When SNR is $10dB - 30dB$, B-CEM is proved to be the most effective detector because its corresponding AUC value of (P_D, P_F) is obviously the highest. With the increase of SNR, the corresponding AUC value of (P_D, τ) and (P_F, τ) for B-CEM increases, and $AUC_{(D,\tau)}$ of B-CEM is the highest when SNR is $20dB$ and $30dB$. Therefore, the detection probability of B-CEM increases with the increase of SNR and is

the highest when SNR is $20dB$ and $30dB$. While background suppression of B-CEM decreases with the increase of SNR. Since we first acquire the approximate posterior distribution over the true target spectrum, and then the approximate true target spectrum \mathbf{t} is randomly sampled from the obtained distribution. There is some uncertainty in this process, which is the reason why background suppression of B-CEM is worse than that of some other detectors.

Generally, distributional estimates adopted in B-CEM present a significant performance boost in the case of noise or spectral inconsistency compared to other detectors.

2) *Detection performance on the AVIRIS Cuprite data set:* The corresponding numerical AUC with the noisy known target spectrum for all detectors are reported in Table III in detail. Figure 10 and Figure 11 show the detection results and ROC Curve on the AVIRIS Cuprite data set with the noisy known target spectrum when the SNR (Signal-to-Noise Ratio) ranges from $10dB - 30dB$.

TABLE III: AUC of the Different Methods on the Cuprite Data Set. The known spectrum of the target \mathbf{t}_{obs} contains Gaussian white noise of SNR ranges in $10dB - 50dB$. Best results are highlighted in bold.

| | SNR = 10 | SNR = 20 | SNR = 30 | SNR = 40 | SNR = 50 |
|--------------|-----------------|-----------------|-----------------|-----------------|-----------------|
| CEM [27] | 42.65 | 50.19 | 72.13 | 71.17 | 72.78 |
| ACE [18] | 45.79 | 46.62 | 59.22 | 68.69 | 77.08 |
| MF [15] | 43.33 | 50.38 | 73.65 | 72.68 | 75.17 |
| SID [13] | 62.80 | 58.88 | 60.62 | 60.56 | 60.73 |
| SAM [12] | 59.07 | 56.74 | 58.84 | 59.02 | 59.20 |
| E-CEM [30] | 63.24 | 80.22 | 79.48 | 81.65 | 80.46 |
| B-CEM | 89.60 | 91.44 | 93.43 | 91.50 | 91.40 |

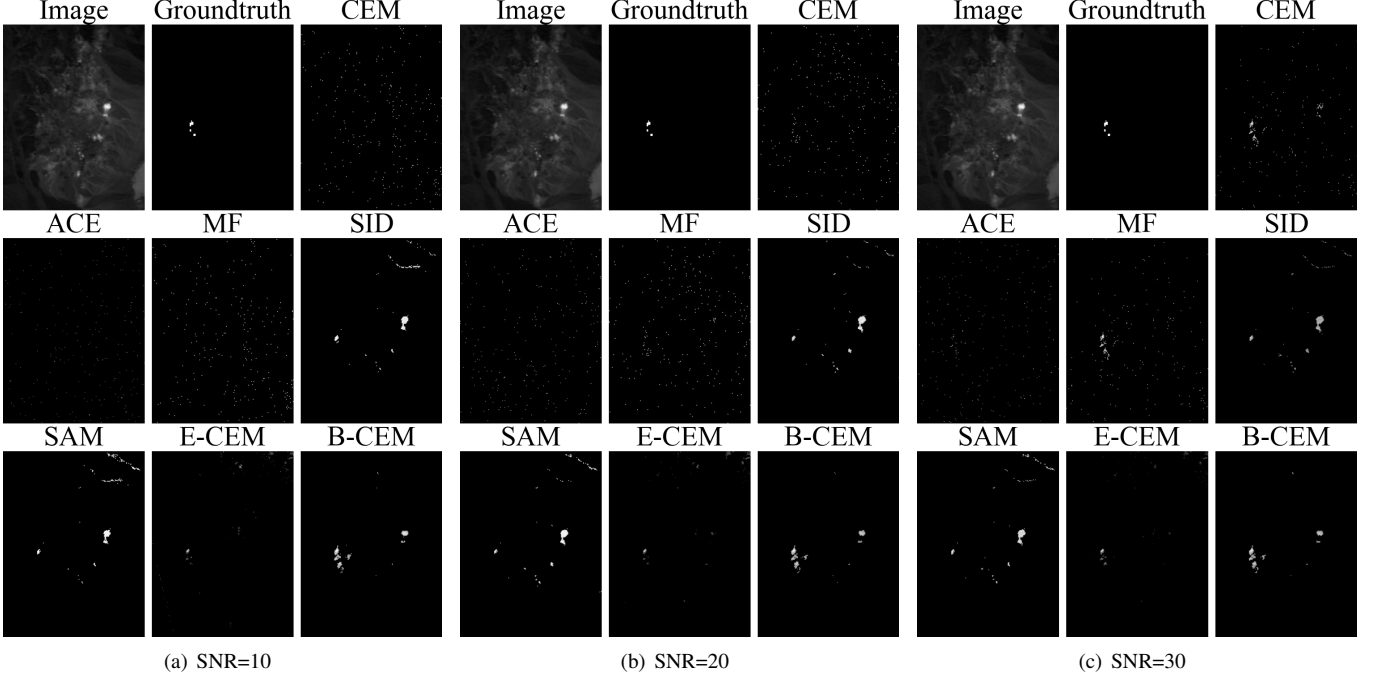


Fig. 10: The detection results of detectors on the AVIRIS Cuprite data set with the noisy known target spectrum. SNR (Signal-to-Noise Ratio) ranges from $10dB - 30dB$.

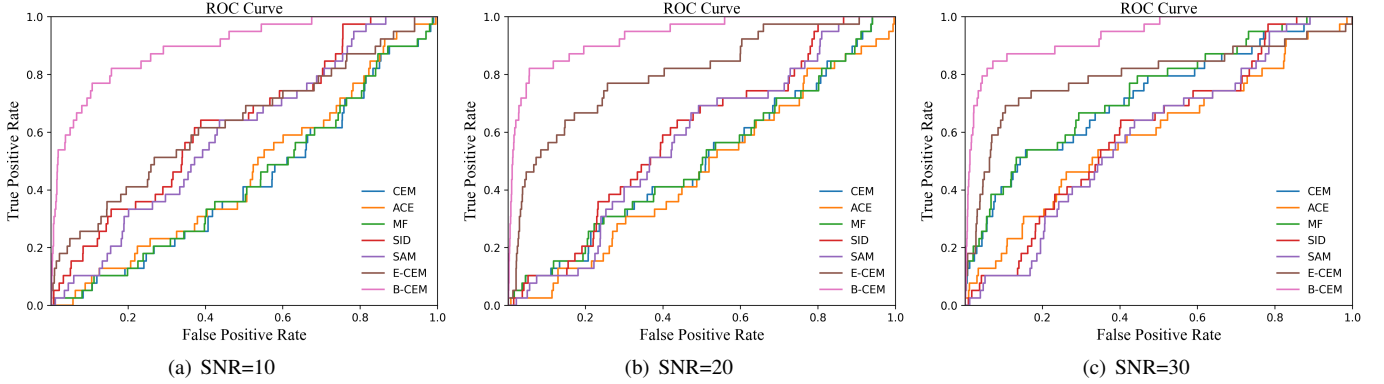


Fig. 11: The ROC Curves of detectors on the AVIRIS Cuprite data set with the noisy known target spectrum. SNR (Signal-to-Noise Ratio) ranges from $10dB - 30dB$.

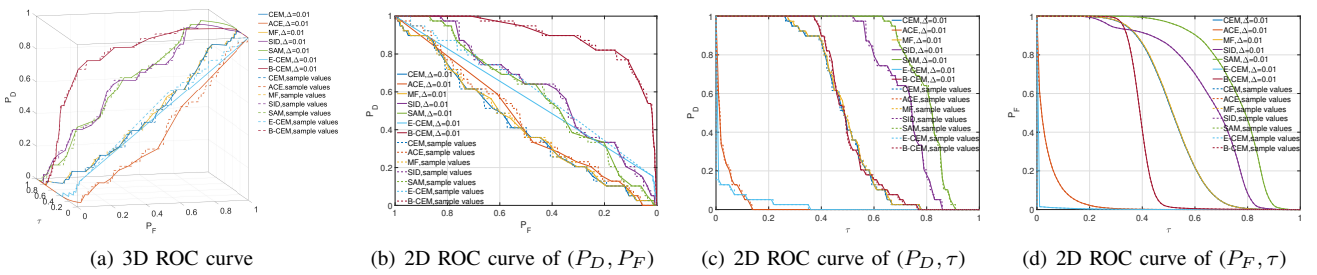


Fig. 12: 3D ROC curves along with its generated three 2D ROC curves using Equation 13 by data sample values and uniform step size, $\Delta = 0.01$, on the Cuprite Data Set with the noisy known target spectrum when $SNR = 10$

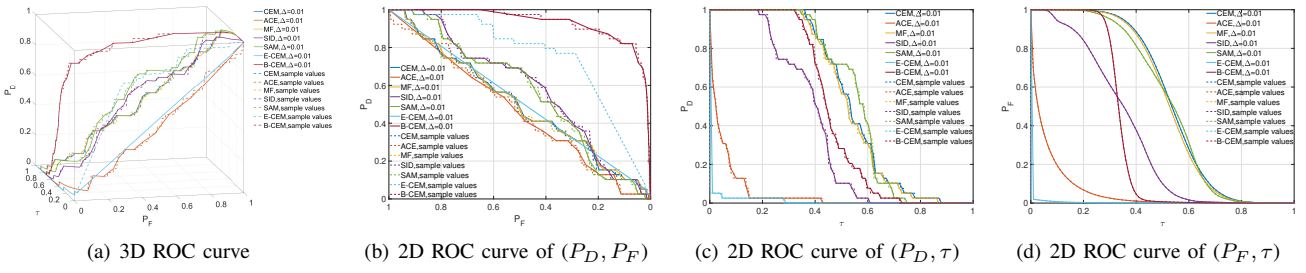


Fig. 13: 3D ROC curves along with its generated three 2D ROC curves using Equation 13 by data sample values and uniform step size, $\Delta = 0.01$, on the Cuprite Data Set with the noisy known target spectrum when $\text{SNR} = 20$

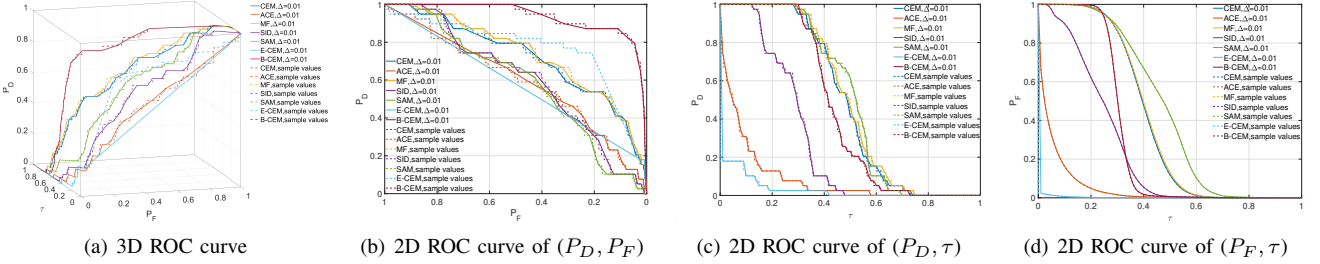


Fig. 14: 3D ROC curves along with its generated three 2D ROC curves using Equation 13 by data sample values and uniform step size, $\Delta = 0.01$, on the Cuprite Data Set with the noisy known target spectrum when $\text{SNR} = 30$

Similarly, the AUC of B-CEM is a significant improvement over that of other detectors. Its AUC also generally conforms to the trend of increasing first and then decreasing. The target spectrum that contains noise of a quite low SNR (for example, 10dB) may lead to the obtained approximation posterior distribution of the true target spectrum is noisy, which further leads to the true target spectrum sampled is noisy, and then leads to the performance decline of the B-CEM detector. While the target spectrum with a quite high SNR (for example, 50dB) is close to the known target spectrum, which is considered as the true target spectrum. Therefore, our hypothesis that the known target spectrum is not consistent with the true spectrum is not valid. Generally, compared with other detectors, B-CEM has a significantly better and relatively robust detection performance regardless of the SNR.

For the visualization of the detection results, B-CEM can detect almost all targets with relatively high confidence. False alarm decreases with the increase of SNR. Besides, Receiver Operating Characteristic (ROC) Curve is shown in Figure 11 and proves the effectiveness of the proposed B-CEM detector. The performance of B-CEM when SNR is 30dB and 20dB is superior to that when SNR is 10dB. Regardless of the SNR of noise added, B-CEM acquires better performance compared to other detectors.

To further evaluate the detection performance of B-CEM, we adopt the 3D ROC curves proposed in [47]. Using $\delta_{\text{normalized}}^{\text{NP}}(\mathbf{t}_{\text{obs}})$ in Equation 13 to threshold the detection maps produced Figure 12-14(a-d).

When SNR is 10dB – 30dB, the AUC value of (P_D, P_F) for B-CEM is the highest, which demonstrates that B-CEM is the most effective detector. With the increase of SNR, the corresponding AUC value of (P_D, τ) and (P_F, τ) for all detectors decrease. Obviously, it is reasonable that background

TABLE IV: AUC of the Different Methods on the synthetic hyperspectral image. The known spectrum of the target \mathbf{t}_{obs} contains Gaussian white noise of SNR ranges in 10dB – 50dB. Best results are highlighted in bold.

| | $\text{SNR} = 10$ | $\text{SNR} = 20$ | $\text{SNR} = 30$ | $\text{SNR} = 40$ | $\text{SNR} = 50$ |
|------------|-------------------|-------------------|-------------------|-------------------|-------------------|
| CEM [27] | 0.00 | 0.00 | 100.00 | 100.00 | 100.00 |
| ACE [18] | 78.36 | 83.60 | 85.87 | 88.22 | 88.74 |
| MF [15] | 0.00 | 0.00 | 100.00 | 100.00 | 100.00 |
| SID [13] | 100.00 | 100.00 | 100.00 | 100.00 | 100.00 |
| SAM [12] | 100.00 | 100.00 | 100.00 | 100.00 | 100.00 |
| E-CEM [30] | 100.00 | 100.00 | 99.98 | 100.00 | 100.00 |
| B-CEM | 100.00 | 100.00 | 100.00 | 99.95 | 100.00 |

suppression decreases with the increase of SNR. However, the less noise actually reduces the detection probability of all detectors. The probable reason can be: 1) The AVIRIS Cuprite data set is mislabeled, or 2) The added Gaussian white noise with a higher SNR makes the target spectrum even closer to that of some other material.

Generally, B-CEM presents better performance in the case of noise or spectral inconsistency compared to other detectors.

3) *Detection performance on the Synthetic Hyperspectral Image:* The numerical AUC with the noisy known target spectrum for all detectors on the synthetic hyperspectral image are reported in Table IV in detail. Figure 15 and Figure 16 show the detection results and ROC Curve with the noisy known target spectrum when the SNR (Signal-to-Noise Ratio) range from 10dB – 30dB.

In general, from Table IV, it can be observed that most detectors perform well when SNR is high. The AUC of detectors including CEM [27], ACE [18], and MF [15] decrease as SNR decreases. When SNR ranging from 10dB – 50dB, the

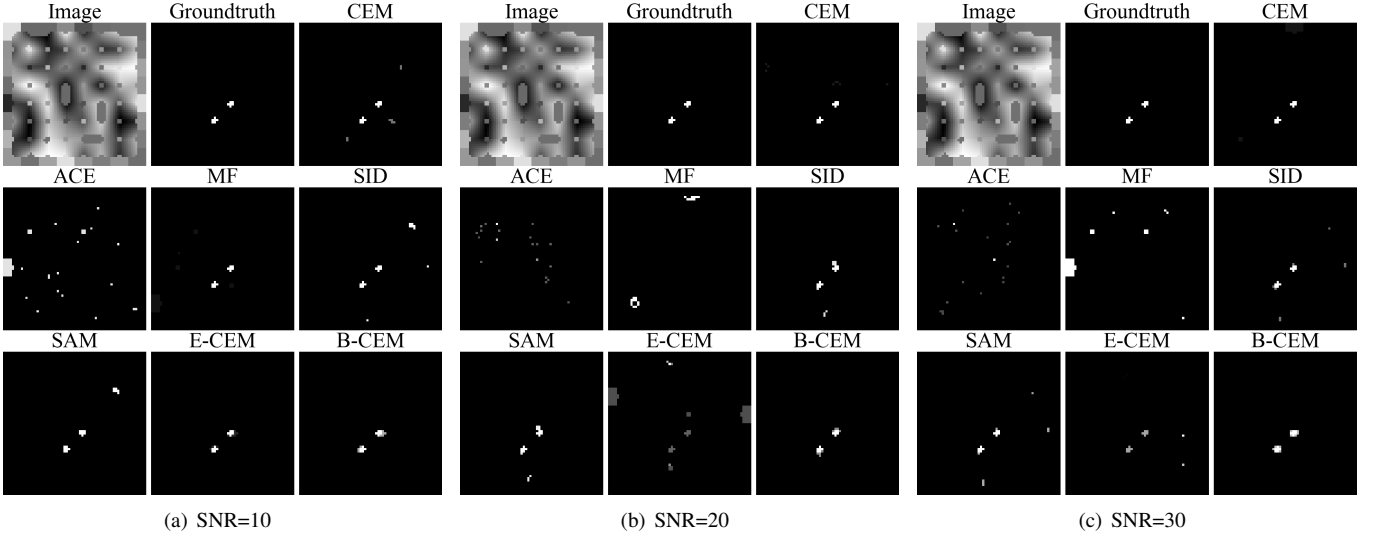


Fig. 15: The detection results of detectors on the synthetic hyperspectral image with the noisy known target spectrum. SNR (Signal-to-Noise Ratio) ranges from $10dB - 30dB$.

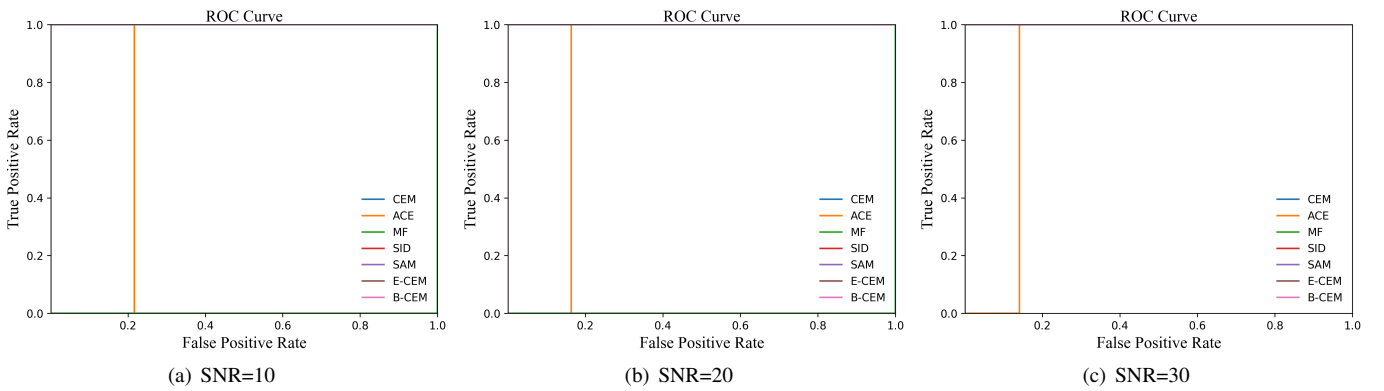


Fig. 16: The ROC Curves of detectors on the synthetic hyperspectral image with the noisy known target spectrum. SNR (Signal-to-Noise Ratio) ranges from $10dB - 30dB$.

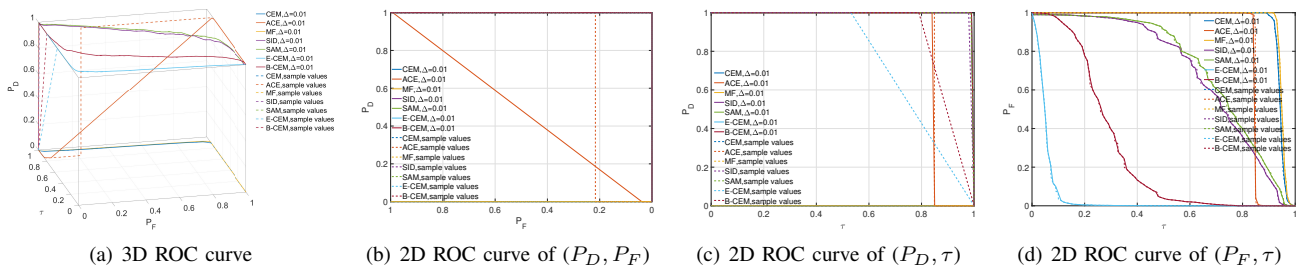


Fig. 17: 3D ROC curves along with its generated three 2D ROC curves using Equation 13 by data sample values and uniform step size, $\Delta = 0.01$, on the synthetic hyperspectral image with the noisy known target spectrum when $\text{SNR} = 10$

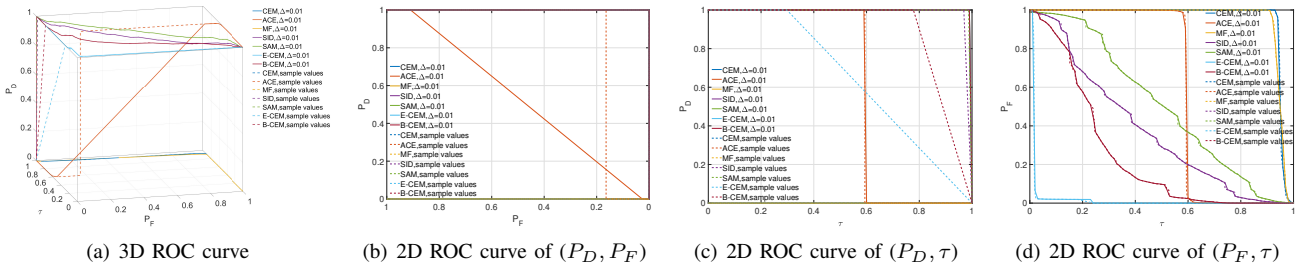


Fig. 18: 3D ROC curves along with its generated three 2D ROC curves using Equation 13 by data sample values and uniform step size, $\Delta = 0.01$, on the synthetic hyperspectral image with the noisy known target spectrum when $\text{SNR} = 20$

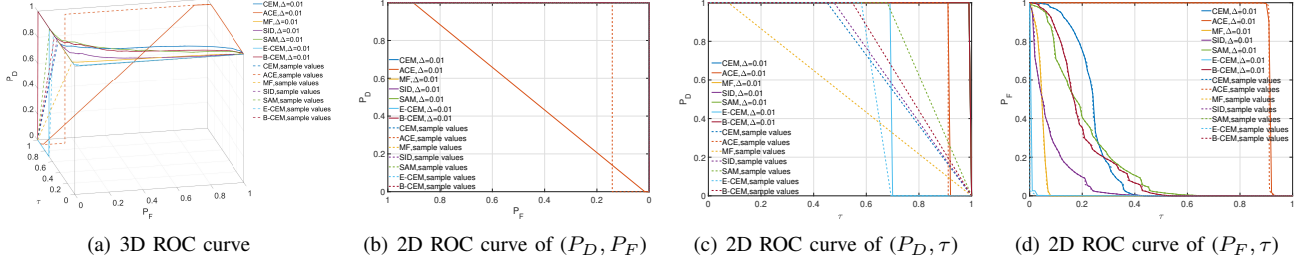


Fig. 19: 3D ROC curves along with its generated three 2D ROC curves using Equation 13 by data sample values and uniform step size, $\Delta = 0.01$, on the synthetic hyperspectral image with the noisy known target spectrum when $\text{SNR} = 30$

performance on synthetic data sets of the same detector at the same noise level is better than that on real data sets. Their good performance on the synthetic hyperspectral image is in sharp contrast to their relatively poor performance on the two real hyperspectral images, namely the AVIRIS San Diego data set and the AVIRIS Cuprite data set. Since the primary difference between synthetic images and real images is the reliability of the known target spectrum, the known target spectrum of the synthetic image is reliable and can be regarded as the true target spectrum. Therefore, the better performance of most detectors on the synthetic data set exactly proves that the true target spectrum is crucial for target detection performance. Once the true target spectrum is obtained, the detectors can not only achieve better detection performance but also achieve stronger robustness to noise.

The 2D ROC Curve of B-CEM is the same as that of CEM [27], SID [13], SAM [12] and E-CEM [30], as shown in Figure 16. However, their performance variations are presented in Figure 17-19(a-d), which is produced by thresholding the detection maps via $\delta_{\text{normalized}}^{\text{NP}}(\mathbf{t}_{\text{obs}})$ in Equation 13.

When SNR is $10\text{dB} - 30\text{dB}$, it can be observed that the AUC value of (P_D, P_F) for B-CEM is very high. Therefore, we can draw the conclusion that B-CEM is the most effective detector. The corresponding AUC value of (P_D, τ) hardly changes at different noise levels, which proves that the detection probability of B-CEM is relatively robust to noise. While background suppression of B-CEM increases with the increase of SNR , which is described in Figure 17-19(d). Although background suppression of B-CEM is worse than that of some other detectors due to the distribution estimation adopted, the detection performance of B-CEM is significantly better than that of other detectors.

We can observe the same conclusion from both AUC values

and 2D ROC and 3D ROC curves. Most detectors perform well when adding very little noise. With the decrease of SNR , the performance of other detectors except B-CEM decreased. However, most detectors perform better on synthetic datasets than on real datasets. This also shows the importance of matching the prior spectrum with the target spectrum, so it is necessary to estimate the true spectrum.

Generally, the same conclusions can be drawn from both numerical AUC and ROC curves. Most detectors perform well when SNR is high. Although the performances of all detectors decrease with the decrease of SNR , B-CEM is more robust to noise. Most detectors perform better on synthetic data sets than on real data sets at the same noise level. This indicates the significance of the true target spectrum. Therefore, estimating the true target spectrum is necessary, which might be the primary reason for the B-CEM's effectiveness.

B-CEM is suitable for the application scenario where the known target spectrum contains noise or the gap between the true target spectrum and the known target spectrum exists. For example, the proposed method can acquire a better performance when the sensor, surface contaminants, material diversity, light shadows, weather, or other environmental factors of capturing hyperspectral images to be detected are quite different from those of obtaining the known target spectrum. However, when the difference between the true target spectrum and the known target spectrum is quite small, or when the true target spectrum is available, the true target spectrum that we obtained by distribution estimation may deviate from the known true target spectrum due to the inherent uncertainty of distribution estimation. Therefore, the point estimation might be a better choice when the true target spectrum is available.

IV. CONCLUSION

We propose a Bayesian Constrained Energy Minimization method (B-CEM) for hyperspectral target detection, where we introduce the true target spectrum as an intermediate variable and build a hierarchical probability model. Given the characteristics of hyperspectral image and target detection task, we adopt the Dirichlet distribution to approximate the posterior distribution of the true target spectrum. The validity of the proposed B-CEM and the necessity to obtain the true target spectrum are proved by experimental results on three data sets. The proposed B-CEM detector gets noticeable improvements and is relatively robust, especially when the known target spectrum is noisy or inconsistent with the true target spectrum. Furthermore, B-CEM may provide new ideas for further studies on hyperspectral target detection when the known target spectrum is less reliable.

ACKNOWLEDGMENT

The authors would like to specifically thank Dr. Chang for his paper "An Effective Evaluation Tool for Hyperspectral Target Detection: 3D Receiver Operating Characteristic Curve Analysis" and the 2D/3D ROC software codes that this paper guided to get. The 2D/3D ROC software codes are provided by the website of the Remote Sensing Signal and Image Processing Laboratory (RSSIPL), University of Maryland, Baltimore County (UMBC), <https://wiki.umbc.edu/display/rssipl/10.+Download>.

REFERENCES

- [1] G. Cheng, J. Han, and X. Lu, "Remote sensing image scene classification: Benchmark and state of the art," *Proceedings of the IEEE*, vol. 105, no. 10, pp. 1865–1883, 2017.
- [2] X. Kang, X. Zhang, S. Li, K. Li, J. Li, and J. A. Benediktsson, "Hyperspectral anomaly detection with attribute and edge-preserving filters," *IEEE Transactions on Geoscience and Remote Sensing*, vol. 55, no. 10, pp. 5600–5611, 2017.
- [3] X. Kang, Y. Huang, S. Li, H. Lin, and J. A. Benediktsson, "Extended random walker for shadow detection in very high resolution remote sensing images," *IEEE Transactions on Geoscience and Remote Sensing*, vol. 56, no. 2, pp. 867–876, 2018.
- [4] B. Horig, F. Kuhn, F. Oschutz, and F. Lehmann, "Hymap hyperspectral remote sensing to detect hydrocarbons," *International Journal of Remote Sensing*, vol. 22, no. 8, pp. 1413–1422, 2001.
- [5] B. Datt, T. McVicar, T. Van Niel, D. Jupp, and J. Pearlman, "Preprocessing eo-1 hyperspectral data to support the application of agricultural indexes," *IEEE Transactions on Geoscience and Remote Sensing*, vol. 41, no. 6, pp. 1246–1259, 2003.
- [6] K. Tiwari, M. Arora, and D. Singh, "An assessment of independent component analysis for detection of military targets from hyperspectral images," *International Journal of Applied Earth Observation and Geoinformation*, vol. 13, no. 5, pp. 730–740, 2011.
- [7] D. Manolakis and G. Shaw, "Detection algorithms for hyperspectral imaging applications," *IEEE Signal Processing Magazine*, vol. 19, no. 1, pp. 29–43, 2002.
- [8] C. Lin, S.-Y. Chen, C.-C. Chen, and C.-H. Tai, "Detecting newly grown tree leaves from unmanned-aerial-vehicle images using hyperspectral target detection techniques," *ISPRS Journal of Photogrammetry and Remote Sensing*, vol. 142, pp. 174–189, 2018.
- [9] M. Rahimzadegan, B. Sadeghi, M. Masoumi, and S. Taghizadeh Ghalehjoghi, "Application of target detection algorithms to identification of iron oxides using aster images: a case study in the north of semnan province, iran," *Arabian Journal of Geosciences*, vol. 8, pp. 7321–7331, Sep 2015.
- [10] M. L. Pieper, D. Manolakis, E. Truslow, T. Cooley, and M. Brueggeman, "False alarm mitigation techniques for hyperspectral target detection," in *Algorithms and Technologies for Multispectral, Hyperspectral, and Ultraspectral Imagery XIX* (S. S. Shen and P. E. Lewis, eds.), vol. 8743, pp. 19 – 30, International Society for Optics and Photonics, SPIE, 2013.
- [11] M. T. Eismann, A. D. Stocker, and N. M. Nasrabadi, "Automated hyperspectral cueing for civilian search and rescue," *Proceedings of the IEEE*, vol. 97, no. 6, pp. 1031–1055, 2009.
- [12] F. Kruse, A. Lefkoff, J. Boardman, K. Heidebrecht, A. Shapiro, P. Barloon, and A. Goetz, "The spectral image processing system (sips)—interactive visualization and analysis of imaging spectrometer data," *Remote Sensing of Environment*, vol. 44, no. 2, pp. 145–163, 1993. Airbone Imaging Spectrometry.
- [13] C.-I. Chang, "An information-theoretic approach to spectral variability, similarity, and discrimination for hyperspectral image analysis," *IEEE Transactions on Information Theory*, vol. 46, no. 5, pp. 1927–1932, 2000.
- [14] T. Wang, B. Du, and L. Zhang, "An Automatic Robust Iteratively Reweighted Unstructured Detector for Hyperspectral Imagery," *IEEE Journal of Selected Topics in Applied Earth Observations and Remote Sensing*, vol. 7, pp. 2367–2382, June 2014.
- [15] D. Manolakis, R. Lockwood, T. Cooley, and J. Jacobson, "Is there a best hyperspectral detection algorithm?," in *Algorithms and Technologies for Multispectral, Hyperspectral, and Ultraspectral Imagery XV* (S. S. Shen and P. E. Lewis, eds.), vol. 7334 of *Society of Photo-Optical Instrumentation Engineers (SPIE) Conference Series*, p. 733402, May 2009.
- [16] F. Robey, D. Fuhrmann, E. Kelly, and R. Nitzberg, "A cfar adaptive matched filter detector," *IEEE Transactions on Aerospace and Electronic Systems*, vol. 28, no. 1, pp. 208–216, 1992.
- [17] W.-S. Chen and I. S. Reed, "A new cfar detection test for radar," *Digital Signal Processing*, vol. 1, no. 4, pp. 198–214, 1991.
- [18] S. Kraut and L. Scharf, "The cfar adaptive subspace detector is a scale-invariant glrt," *IEEE Transactions on Signal Processing*, vol. 47, no. 9, pp. 2538–2541, 1999.
- [19] S. Kraut, L. Scharf, and L. McWhorter, "Adaptive subspace detectors," *IEEE Transactions on Signal Processing*, vol. 49, no. 1, pp. 1–16, 2001.
- [20] D. Manolakis, D. Marden, and G. A. Shaw, "Hyperspectral image processing for automatic target detection applications," *LINCOLN LABORATORY JOURNAL*, vol. 14, no. 1, pp. 79–116, 2003.
- [21] C.-I. Chang, "Hyperspectral target detection: Hypothesis testing, signal-to-noise ratio, and spectral angle theories," *IEEE Transactions on Geoscience and Remote Sensing*, pp. 1–23, 2021.
- [22] J. Harsanyi and C.-I. Chang, "Hyperspectral image classification and dimensionality reduction: an orthogonal subspace projection approach," *IEEE Transactions on Geoscience and Remote Sensing*, vol. 32, no. 4, pp. 779–785, 1994.
- [23] S. Bernabé, S. Sánchez, A. Plaza, S. López, J. A. Benediktsson, and R. Sarmiento, "Hyperspectral unmixing on gpus and multi-core processors: A comparison," *IEEE Journal of Selected Topics in Applied Earth Observations and Remote Sensing*, vol. 6, no. 3, pp. 1386–1398, 2013.
- [24] C.-I. Chang and J. Chen, "Orthogonal subspace projection using data sphering and low-rank and sparse matrix decomposition for hyperspectral target detection," *IEEE Transactions on Geoscience and Remote Sensing*, pp. 1–19, 2021.
- [25] Y. Chen, N. M. Nasrabadi, and T. D. Tran, "Sparse representation for target detection in hyperspectral imagery," *IEEE Journal of Selected Topics in Signal Processing*, vol. 5, no. 3, pp. 629–640, 2011.
- [26] Y. Chen, N. M. Nasrabadi, and T. D. Tran, "Simultaneous joint sparsity model for target detection in hyperspectral imagery," *IEEE Geoscience and Remote Sensing Letters*, vol. 8, no. 4, pp. 676–680, 2011.
- [27] W. Farrand, "Mapping the distribution of mine tailings in the Coeur d'Alene River Valley, Idaho, through the use of a constrained energy minimization technique," *Remote Sensing of Environment*, vol. 59, pp. 64–76, Jan. 1997.
- [28] S. Yang, Z. Shi, and W. Tang, "Robust hyperspectral image target detection using an inequality constraint," *IEEE Transactions on Geoscience and Remote Sensing*, vol. 53, no. 6, pp. 3389–3404, 2015.
- [29] Z. Zou and Z. Shi, "Hierarchical suppression method for hyperspectral target detection," *IEEE Transactions on Geoscience and Remote Sensing*, vol. 54, no. 1, pp. 330–342, 2016.
- [30] R. Zhao, Z. Shi, Z. Zou, and Z. Zhang, "Ensemble-based cascaded constrained energy minimization for hyperspectral target detection," *Remote Sensing*, vol. 11, p. 1310, June 2019.

- [31] H. Ren and C.-I. Chang, "Automatic spectral target recognition in hyperspectral imagery," *IEEE Transactions on Aerospace and Electronic Systems*, vol. 39, no. 4, pp. 1232–1249, 2003.
- [32] Z. Wang and J.-H. Xue, "Matched shrunken subspace detectors for hyperspectral target detection," *Neurocomputing*, vol. 272, pp. 226–236, 2018.
- [33] X. Yang, J. Chen, and Z. He, "Sparse-SpatialCEM for Hyperspectral Target Detection," *IEEE Journal of Selected Topics in Applied Earth Observations and Remote Sensing*, vol. 12, pp. 2184–2195, July 2019.
- [34] J. F. Randrianasoa, P. Cettour-Janet, C. Kurtz, Éric Desjardin, P. Gançarski, N. Bednarek, F. Rousseau, and N. Passat, "Supervised quality evaluation of binary partition trees for object segmentation," *Pattern Recognition*, vol. 111, p. 107667, 2021.
- [35] S. Yang and Z. Shi, "Hyperspectral image target detection improvement based on total variation," *IEEE Transactions on Image Processing*, vol. 25, no. 5, pp. 2249–2258, 2016.
- [36] Y. Xu, Q. Du, and N. H. Younan, "Particle swarm optimization-based band selection for hyperspectral target detection," *IEEE Geoscience and Remote Sensing Letters*, vol. 14, no. 4, pp. 554–558, 2017.
- [37] C.-I. Chang and S. Wang, "Constrained band selection for hyperspectral imagery," *IEEE Transactions on Geoscience and Remote Sensing*, vol. 44, no. 6, pp. 1575–1585, 2006.
- [38] Y. Dong, B. Du, and L. Zhang, "Target detection based on random forest metric learning," *IEEE Journal of Selected Topics in Applied Earth Observations and Remote Sensing*, vol. 8, no. 4, pp. 1830–1838, 2015.
- [39] T. Guo, F. Luo, L. Zhang, B. Zhang, X. Tan, and X. Zhou, "Learning structurally incoherent background and target dictionaries for hyperspectral target detection," *IEEE Journal of Selected Topics in Applied Earth Observations and Remote Sensing*, vol. 13, pp. 3521–3533, 2020.
- [40] G. Camps-Valls, "Kernel spectral angle mapper," *Electronics Letters*, vol. 52, pp. 1218–1220, July 2016.
- [41] L. Yan, M. Zhao, X. Wang, Y. Zhang, and J. Chen, "Object detection in hyperspectral images," *IEEE Signal Processing Letters*, vol. 28, pp. 508–512, 2021.
- [42] L. He, J. Li, C. Liu, and S. Li, "Recent advances on spectral-spatial hyperspectral image classification: An overview and new guidelines," *IEEE Transactions on Geoscience and Remote Sensing*, vol. 56, no. 3, pp. 1579–1597, 2018.
- [43] Z. Zou, Z. Shi, J. Wu, and H. Wang, "Quadratic constrained energy minimization for hyperspectral target detection," in *2015 IEEE International Geoscience and Remote Sensing Symposium (IGARSS)*, pp. 4979–4982, 2015.
- [44] R. N. Clark, G. A. Swayze, A. J. Gallagher, T. V. King, and W. M. Calvin, "The u. s. geological survey, digital spectral library: Version 1: 0.2 to 3.0 μm ," tech. rep., 1993. Report.
- [45] Y.-C. C. Chang, H. Ren, C.-I. Chang, and R. S. Rand, "How to design synthetic images to validate and evaluate hyperspectral imaging algorithms," in *Algorithms and Technologies for Multispectral, Hyperspectral, and Ultraspectral Imagery XIV* (S. S. Shen and P. E. Lewis, eds.), vol. 6966 of *Society of Photo-Optical Instrumentation Engineers (SPIE) Conference Series*, p. 69661P, Apr. 2008.
- [46] R. N. Clark, G. A. Swayze, K. E. Livo, R. F. Kokaly, S. J. Sutley, J. B. Dalton, R. R. McDougal, and C. A. Gent, "Imaging spectroscopy: Earth and planetary remote sensing with the USGS Tetracorder and expert systems," *Journal of Geophysical Research (Planets)*, vol. 108, p. 5131, Dec. 2003.
- [47] C.-I. Chang, "An effective evaluation tool for hyperspectral target detection: 3d receiver operating characteristic curve analysis," *IEEE Transactions on Geoscience and Remote Sensing*, vol. 59, no. 6, pp. 5131–5153, 2021.